Extended regulation interface coupled to the allosteric network and disease mutations in the PP2A-B56δ holoenzyme

Cheng-Guo Wu[1,2], Vijaya K. Balakrishnan[1], Pankaj S. Parihar[1], Kirill Konovolov[3], Yu-Chia Chen[1,4], Ronald A Merrill[5], Hui Wei[6], Bridget Carragher[6], Ramya Sundaresan[1], Qiang Cui[7], Brian E. Wadzinski[8], Mark R. Swingle[9], Alla Musiyenko[9], Richard Honkanen[9], Wendy K. Chung[10], Aussie Suzuki[1,2,5], Stefan Strack[5], Xuhui Huang[2,3], Yongna Xing[1,2,*]

[1]McArdle Laboratory for Cancer Research, Department of Oncology, University of Wisconsin at Madison, School of Medicine and Public Health, Madison, Wisconsin 53705, USA

[2]Biophysics program, University of Wisconsin at Madison, Wisconsin 53706, USA

[3]Chemistry Department, University of Wisconsin at Madison, Wisconsin 53706, USA

[4]Molecular and Cellular Pharmacology program, University of Wisconsin at Madison, Wisconsin 53706, USA

[5]Department of Neuroscience and Pharmacology, University of Iowa, Iowa City, IA 52242, USA

[6]New York Structural biology Center, New York, NY 10027, USA

[7]Department of Chemistry, Metcalf Center for Science & Engineering, Boston University, Boston, MA 02215, USA

[8]Department of Pharmacology, Vanderbilt University, Nashville, TN 37232, USA

[9]Department of Biochemistry and Molecular Biology, University of South Alabama, Mobile, AL 36688, USA

[10]Departments of Pediatrics and Medicine, Columbia University, New York, NY 10032, USA

[*]To whom correspondence should be addressed:

Yongna Xing

E-mail: xing@oncology.wisc.edu;

Phone: 608-262-8376

Fax: 608-262-2824

Abstract

An increasing number of mutations associated with devastating human diseases are diagnosed by whole-genome/exon sequencing. Recurrent *de novo* missense mutations have been discovered in B56δ (encoded by *PPP2R5D*), a regulatory subunit of protein phosphatase 2A (PP2A), that cause intellectual disabilities (ID), macrocephaly, Parkinsonism, and a broad range of neurological symptoms. Single-particle cryo-EM structures show that the PP2A-B56δ holoenzyme possesses closed latent and open active forms. In the closed form, the long, disordered arms of B56δ termini fold against each other and the holoenzyme core, establishing dual autoinhibition of the phosphatase active site and the substrate-binding protein groove. The resulting interface spans over 190 Å and harbors unfavorable contacts, activation phosphorylation sites, and nearly all residues with ID-associated mutations. Our studies suggest that this dynamic interface is close to an allosteric network responsive to activation phosphorylation and altered globally by mutations. Furthermore, we found that ID mutations perturb the activation phosphorylation rates, and the severe variants significantly increase the mitotic duration and error rates compared to the wild variant.

Introduction

43

44   Protein phosphatase 2A (PP2A) is a major serine/threonine phosphatase in the PPP family that

45   targets many cellular phosphoproteins via diverse heterotrimeric holoenzymes in mammalian

46   cells[1-6]. Each holoenzyme consists of a common core formed by the scaffolding A and catalytic

47   C (PP2Ac) subunits and a diverse regulatory subunit from one of the four major families

48   (B/B55/PR55 (*PPP2R2*), B'/B56/PR61 (*PPP2R5*), B''/PR72 ((*PPP2R3*), and B'''/Striatin).

49   Whole exome/genome sequencing identified mutations in PP2A subunits in cancer and largely

50   *de novo* mutations in neurological disorders[7-11]. Both unique and recurrent mutations have been

51   found in the common core of the B56 regulatory subunits. Up to 20 recurrent missense mutations

52   in B56δ cause severe intellectual and developmental disorders[8,9,12,13], known as Jordan

53   Syndrome. More recently, multiple missense variants in B56δ have been associated with early-

54   onset Parkinsonism[14-16]. The incidence of neurodevelopmental and neurodegenerative disorders

55   associated with B56δ is estimated at 2.32 to 2.87 per 100,000 births; 250,000 cases are estimated

56   to be undiagnosed[8,9,12,14-16].

57   Recent studies indicate that PP2A holoenzymes from the B56 family recognize a signature short

58   linear motif (SLiM), LxxIxE, in the disordered regions of substrates[17-19]. Diverse SLiMs are

59   found in intrinsically disordered regions that serve as docking interfaces for peptide-binding

60   proteins and play crucial roles in modulating cellular signaling[20,21]. Several SLiMs have been

61   uncovered for the PPP family phosphatases targeting different substrates[22-25]. The B56-targeting

62   LxxIxE SLiM binds to a protein groove in the conserved common core of B56 regulatory

63   subunits[19,26]. Several thousands of B56 SLiM-containing proteins are predicted in the human

64   proteome. Many of these are involved in broad cellular and physiological processes[17]. B56

65 regulatory subunits play essential roles in neurodevelopment, brain functions, and tumor

66 suppression, as reflected by their ability to control cell cycle[17,18,27-29], cytoskeleton dynamics[30],

67 DNA damage responses[31,32], CREB signaling[33], and c-Myc stability[34-38].

68 In addition to the common core, B56δ possesses long disordered regions at the N- and C-termini

69 that harbor multiple phosphorylation sites (Extended Data Figs. 1-2). The PP2A-B56δ

70 holoenzyme is known to be highly regulated by distinct cellular signaling pathways. Protein

71 kinase A (PKA) phosphorylates B56δ and activates the holoenzyme, thereby regulating signaling

72 molecules downstream of cyclic adenosine monophosphate (cAMP)[39-41]. At the G2/M

73 checkpoint, the DNA-responsive checkpoint kinase Chk1 phosphorylates B56δ and stimulates

74 the holoenzyme activity[42]. B56δ also plays a critical role in controlling mitotic exit[43]. Moreover,

75 the B56δ holoenzyme is phosphorylated by the ataxia-telangiectasia mutated (ATM) kinase upon

76 DNA damage and regulates p53 function[44]. Understanding the structure of the PP2A-B56δ

77 holoenzyme and the mechanisms by which it is activated is essential for shedding light on its

78 complex regulation and the pathological mechanisms of its disease mutations.

79 Here we determined a high-resolution cryo-EM structure of a PP2A-B56δ holoenzyme bearing

80 the E197K disease mutation at 2.7 Å. The structure resembles a closed form of the holoenzyme.

81 The long N/C-extensions of B56δ make cross-arm interactions against each other and the

82 holoenzyme core, creating an extended dynamic interface that suppresses both the phosphatase

83 active site and the substrate SLiM-binding groove. Nearly all of the previously identified

84 phosphorylation sites, as well as the residues mutated in individuals with intellectual disabilities

85 (ID), are located at or near this interface. We further demonstrated that ID mutations alter the

86 activation phosphorylation rates in response to cAMP-induced activation of PKA. ID mutations

87   also alter the basal level of SLiM-binding and up to a quarter of critical cellular signaling

88   endpoints that affect cell cycle progression and mitotic defects during cell division that could

89   help explain macrocephaly observed in humans. Our studies reveal a coherent allosteric network

90   crucial for phosphorylation-mediated B56δ holoenzyme activation that is altered globally by ID

91   mutations.

Results

Overall cryo-EM structures of the PP2A-B56δ holoenzyme

94   Structure determination of the PP2A-B56δ holoenzyme by single-particle cryo-EM turned out to

95   be highly challenging. We explored the "spotiton" technology[45,46] to capture the dynamic states

96   of the holoenzyme on the grids. The spotiton grids "purified' a closed form of the holoenzyme

97   by dissociating the majority of the holoenzyme particles (Extended Data Fig. 3a). Albeit this

98   form represents a small fraction of total particles, it gave a 4 Å map with uniform density for the

99   long disordered regions at the N/C-termini (Extended Data Fig. 3b). We further explored

100   glutaraldehyde and EDC (ethyl carbodiimide) crosslinks and tested different detergents and EM

101   grids to control ice thickness and particle behavior. Nonetheless, the cryo-EM data for the

102   crosslinked holoenzyme failed to capture any closed forms. Next, we examined the holoenzyme

103   bearing different ID mutations. After an extensive effort, we revealed two major forms for the

104   E197K variant of the holoenzyme: a closed form with a map of 2.59 Å and a loose form with a

105   map of 3.13 Å (Extended Data Fig. 4). The crystal structure of the PP2A-B56γ1 holoenzyme

106   (PDB code: 2NYL)[47,48], which represents the common core for the B56 family (Extended Data

107   Fig. 1), fits the map for the B56δ holoenzyme core quite well. Since the N/C-arms are invisible

108   in the loose form, we next focused on the structure of the closed form of the holoenzyme.

109   The building of the N/C-arms in the closed form was guided by XL-MS (crosslink mass

110   spectrometry). Using zero-length EDC crosslink followed by multiple protease digestions and

111   MS runs, two crosslinked residue pairs in the N/C-arms gave detection frequency comparable to

112   or better than those in the holoenzyme core (Extended Data Fig. 5). The structure of the closed

113   form was refined at 2.7 Å (Extended data Table 1 and Extended Data Fig. 4 and 6). It reveals

114   extensive cross-arm interactions between the disordered regions of the B56δ termini; they

115   interact with the holoenzyme core along a long path that spans over 190 Å (Fig. 1). While the

116   long, linear interface involving two remote disordered arms is intrinsically dynamic in nature, it

117   also harbors a significant number of unfavorable contacts (Fig. 1b), underlying an unprecedented

118   super-long dynamic interface in this highly regulated holoenzyme.

119   **The super-dynamic interface in the PP2A-B56δ holoenzyme**

120   The above long-distance interface in the PP2A-B56δ holoenzyme centers at the N/C-arm

121   crossover and makes close contacts with the PP2A catalytic subunit (PP2Ac) and the internal

122   loop of B56 (B56-IL) (I) (Fig. 1b and Extended Data Fig. 7a). The N/C-arms are juxtaposed

123   against each other toward the termini and make close contacts with the B56δ core (II) (Fig. 1b

124   and Extended Data Fig. 7b). Diverging from the crossover and perpendicular to the juxtaposed

125   lower N/C-arms, the upper C-arm makes rich hydrophobic contacts with PP2Ac and

126   miscellaneous contacts with the B56δ core and B56-IL (III) (Fig. 1b and Extended Data Fig. 7c);

127   at the other side, the upper N-arm passes through the cleft between the A-subunit and the B56δ

128   core and makes different modes of contacts with both (IV) (Fig. 1b and Extended Data Fig. 7d).

129   Intriguingly, the N/C-arm crossover is most rich in repulsive contacts (Fig. 1b). Most

130   prominently, E200 in B56-IL makes repulsive contacts to D578 in the C-arm and unfavorable

131   contacts to several hydrophobic residues in the N/C-arms, I72, Y74, and I582 (Fig. 2a). In

132   addition, E84 in the N-arm makes unfavorable contacts with Y580, a hydrophobic residue in the

133   C-arm (Fig. 2a). These repulsive contacts, together with the energetically unfavorable bending of

134   the N/C-arms, make the crossover the "hottest" hubs along the extended dynamic interface.

135   Other unfavorable contacts involve a nearby residue R86 in the upper N-arm (Fig. 2a). The

136   E197K ID mutation creates two repulsive contacts to R571 and K73 in the C-arm and N-arm,

137   respectively (Fig. 2a). Such changes might reduce the number of conformational states of the

138   holoenzyme, and thus allowed us to determine the structure of the closed form of the

139   holoenzyme using single-particle cryo-EM.

140   We further mapped the hydrophobic contacts along the dynamic interface (Fig. 2b). While many

141   small patches of hydrophobic contacts intertwine with the above unfavorable contacts, the

142   dominant rich hydrophobic contacts are made by the two visible ends of the C-arm. L568 and

143   L569 in the upper C-arm are nestled in a hydrophobic pocket formed by six PP2Ac residues and

144   make close contacts with F416 from the B56δ core (Fig. 2b, upper right). Near the C-arm's

145   terminus, L595 interacts with I303 and H263 at the B56 SLiM-binding pocket, which is

146   buttressed by contacts between F594 to P64/65/67 in the N-arm (Fig. 2b, lower right). The

147   distinct maps of energetically repulsive and favorable hydrophobic contacts likely dictate the

148   complex regulation of the holoenzyme functions.

149   **Dual autoinhibition of the holoenzyme and roles of the N/C-arms**

150   The PP2A-B56 holoenzymes target specific substrates via the SLiM-binding pocket and the

151   phosphatase active site that are around 30 Å apart (Extended Data Fig. 8). Phospho-substrates

152   containing B56 SLiMs bind to the SLiM -binding pocket, which in turn places the nearby

153   substrate phosphorylation sites close to the PP2A active site. The closed form of the holoenzyme

154   establishes an elegant mechanism of dual autoinhibition, in which E574 and a cis-B56 SLiM

155   ($L_{595}TASQE_{600}$) in the C-arm make close contacts to the PP2A active site and the B56 SLiM-

156   binding groove (Fig. 3a). E574 in the C-arm mimics the substrate phosphate and makes extensive

157   H-bond and salt bridge interactions to basic residues at the PP2A active site (Fig. 3b). We

158   hypothesize that autoinhibition of the holoenzyme is established by both N/C-arms. Consistent

159   with this notion, deletion of the C-arm (1-560 or ΔC) in either the WT holoenzyme or the E200K

160   disease variant drastically increases the phosphatase activity, and the truncation of the N-arm

161   (90-602 or ΔN) also increases the phosphatase activity of both holoenzymes (Fig. 3c). While the

162   binding of the cis-B56 SLiM to the SLiM-binding groove mimics the substrate SLiMs from

163   substrates[19,26], it is also buttressed by the hydrophobic contacts between the upstream F594 with

164   the N-arm (Fig. 3d). Since the holoenzyme is rapidly denatured during isothermal titration

165   calorimetry (ITC), most likely due to the super-dynamic nature of the N/C-arms, we assessed the

166   binding of the GST-tagged substrate SLiMs from CREB[33] and SYT16[17] to the full-length and

167   truncated holoenzymes using pulldown assay (Fig. 3e). Consistent with the dynamic nature of

168   the N/C-arms, we noticed a significant fluctuation in the experimental results. Therefore,

169   we repeated the experiments 25 times using three batches of materials to learn about the dynamic

170   range of the substrate SLiM-binding (Fig. 3f). The calculated P-values showed significant

171   differences between truncated and full-length holoenzymes. Intriguingly, while the truncation of

172   the N-arm increases the phosphatase activity (Fig. 3c), it significantly decreases the binding of

173   substrate SLiMs (Fig. 3e-f). Our data suggested that the N/C arms confer coherent suppression at

174   the phosphatase active site but opposing roles at the substrate SLiM-binding groove. It is likely

175   that the kink on the C-arm stabilized by the N-arm is required for the suppression of the active

176   site but causes structural tension toward the SLiM-binding groove (Fig. 3a). In the absence of the

177   N-arm, the C-arm binds the SLiM-binding groove tighter with a relaxed kink. Its multipartite

178   contacts with the holoenzyme core, particularly hydrophobic contacts, are largely intact (Fig.

179   2b).

Activation phosphorylation

181   In addition to the structural modalities for dual autoinhibition, the N/C-arms are rich in

182   phosphorylation sites (Fig. 3a). Among these sites, S88, S89, S90, and S573 are the most

183   frequently phosphorylated sites according to the PhosphositePlus database (phosphosite.org).

184   S89, S90, and S573 make extensive H-bond interactions with acidic residues in the holoenzyme

185   core, namely E95 from the scaffold A-subunit, D130 in the B56δ core, and E198 in the B56-IL

186   (Fig. 4a). Phosphorylation at all these sites is expected to create repulsive contacts that would

187   disrupt the closed form and stimulate the loosening of the holoenzyme, leading to its activation.

188   Consistently, phosphorylation of mouse B56δ at S566 (corresponding to S573 of human B56δ)

189   was found to be associated with the activation of the holoenzyme[40]. Using an antibody that we

190   developed to specifically recognize B56δ phosphorylation at S573 (Extended Data Fig. 9), we

191   demonstrated a time-dependent increase of pS573 *in vitro* upon co-incubation of PKA and the

192   holoenzyme (Fig. 4b) and in HEK293 cells upon forskolin-induced cAMP/PKA activation (Fig.

193   4c).

194   To detect the conformational changes associated with activation phosphorylation, we developed

195   a split NanoBiT B56δ holoenzyme sensor, in which the SmBiT peptide fragment was inserted in

196   the holoenzyme core immediately downstream of the N-arm and the LgBiT fragment was fused

197   to the C-terminus of the C-arm (Extended Data Fig. 10). The two NanoBiT fragments are

198   spatially separated in the closed form. If the N/C-arms loosen upon activation phosphorylation

199   by PKA, the two fragments can interact and form an active NanoBiT enzyme (Extended Data

200   Fig. 10). By expressing the WT and E198K mutant holoenzymes bearing this holoenzyme

201   conformation sensor in COS-1 cells, we showed that both holoenzymes produced increased

202   NanoBiT luciferase activity in response to forskolin and rolipram, the combination of an adenine

203   cyclase activator and a PDE4 inhibitor that increases intracellular cAMP levels (Fig. 4d). The

204   responses of both WT and E198K were abolished by S573Q, corroborating the notion that pS573

205   is essential for holoenzyme activation.

206   Both our structural observations and biochemical data support a model of holoenzyme activation

207   upon phosphorylation of the N/C-arms (Fig. 4e). Prior to phosphorylation, the holoenzyme

208   prefers a close conformation with crossover interactions of the N/C-arms to establish dual

209   suppression of both the PP2A active site and the B56 SLiM-binding pocket. Upon

210   phosphorylation of the N/C-arms, the repulsive contacts created at the phosphorylation sites

211   drive the N/C-arms from the close conformation to loosen conformations, allowing access to

212   both the phosphatase active site and the B56 SLiM-binding pocket.

213   **Effects of ID mutations on the holoenzyme allosteric network, autoinhibition, and**

214   **activation phosphorylation**

215   We reasoned that the super-dynamic interface in the PP2A-B56δ holoenzyme forms a coherent

216   allosteric network connecting the activation phosphorylation sites and the structural elements for

217   autoinhibition. Intriguingly, nearly all ID residues found in Jordan Syndrome patients are spread

218   throughout this dynamic interface (Fig. 5a). These mutations could allosterically impact the

219   dissociation of the N/C arms to alter the holoenzyme activity. To gain critical insights into this

220   allosteric network, we performed molecular dynamic (MD) simulations of the closed form of the

221   holoenzymes for WT and two highly recurrent variants, E198K and E200K. Our initial ten 100-

222   ns MD simulations were not successful in sampling the dissociations of the N/C arms. We thus

223   adopted an enhanced sampling technique: replica exchange with solute tempering-2 (REST2)[49],

224   in which we included the terminal 8 residues of the N/C-arms in a "hot region". Twenty replicas

225   were run spanning the temperature space from 310K to 600K. These REST2 simulations resulted

226   in a remarkable improvement in conformational sampling, which led to notable fluctuations in

227   the tails and exposed the B56 SLiM-binding pocket, although complete opening of the arms was

228   not observed (Extended Data Fig. 11a and b).

229   The REST2 conformations from the lowest temperature replica were used to compute the

230   allosteric network. The importance of a particular residue in the network was calculated as the

231   number shortest paths that cross the residue and normalized by the maximum. A residue was

232   evaluated as important if its weight in the network, was above a cutoff, defined as 80% of all

233   residue weights in the network (Extended Data Fig. 11c, black dashed line in Fig. 5c and d).

234   Intriguingly, all ID residues in the B56δ core and phosphorylation sites on the N/C-arms are

235   closely integrated into the allosteric network of the holoenzyme (Fig. 5b). Residues F473, I230,

236   and L313 are located on the periphery, and their weight in the network is below the threshold.

237   Either the E198K or the E200K ID mutation alters the residue weights of other ID residues and

238   phosphorylation sites in the allosteric network (Fig. 5c-d), suggesting that ID mutations globally

239   perturb the coherent dual autoinhibition and phosphorylation-induced holoenzyme activation.

240   Assessing the effects of ID mutations on the holoenzyme function, including substrate SLiM

241   binding and activation phosphorylation rates, turned out to be very challenging. The

242   reproducibility between experimental repeats is considerably low. Given the super-dynamic

243   nature of the B56δ holoenzyme, we initiated an effort to critically control the purification

244   procedures, aiming to precisely control the holoenzyme behavior. We tested two different strains

245   of Hi5 host cells, varied the salt concentrations between 50 mM and 150 mM, and compared

246   French press and Dounce in cell disruption. These variations did not lead to any improvement in

247   the holoenzyme behavior and data fluctuation. No difference was observed in the basal level of

248   holoenzyme phosphorylation, either. The super-dynamic nature of the holoenzymes was also

249   reflected by the fact that the holoenzymes rapidly denatured and formed aggregates during ITC

250   (isothermal calorimetry) experiments.

251   Nonetheless, summarizing the results from up to ten batches of WT and mutant holoenzymes

252   from the above effort, we observed a statistically significant increase in substrate SLiM binding

253   by the E198K ID mutation despite the range of data fluctuation (Fig. 5e). E420K also shows a

254   substantial effect on the basal substrate SLiM-binding; in contrast, the E200K and E197K

255   variants gave mild effects (Fig. 5e). Next, we assessed time-dependent changes of pS573 upon

256   forskolin-induced cAMP/PKA activation in WT and CRISPR-edited HEK 293 cells bearing

257   homozygotic E198K, heterozygotic E200K, or homozygotic E420K[50]. While the pS573 level of

258   the WT holoenzyme is increased at a stable rate, the phosphorylation rate of the disease variants

259   fluctuates in a large range among all experimental repeats (Fig.5f). Our data support a notion that

260   the tight coupling of the dynamic interface, the holoenzyme allosteric network, the regulatory

261   structural elements, and ID mutations render the disease mutations to differentially modulate the

262   basal activity and the activation phosphorylation rates of the holoenzyme. These highly

263   intertwined structural and functional connections are expected to be highly sensitive to

264   experimental conditions and cellular signaling contexts.

265   **Effects of B56δ ID mutations on mitosis**

266   B56 SLiMs are predicted in broad signaling proteins involved in different stages of the cell

267   cycle[17]. Building on previous observations of the role of B56δ at the G2/M checkpoint[42] and

268   mitotic exit[43], we examined whether the ID mutations E198K, E200K, or E420K (introduced by

269   CRISPR editing) affect the mitotic duration and fidelity of HEK293 cells. We used high

270   temporal resolution live-cell imaging to monitor the mitotic progression in HEK293 cells with

271   either WT or mutant B56δ (Fig. 6). The stages of mitosis were determined using a far-red SiR-

272   DNA dye. The mitotic duration (from nuclear envelope breakdown (NEBD) to anaphase onset)

273   was 58 ± 12 min (N = 148) in the WT cells, but significantly extended in E198K (66 ± 16 min, N

274   = 162) and E420K (63 ± 12 min, N = 132) mutant cells. Intriguingly, E200K mutant cells

275   exhibited similar duration to WT (55 ± 11 min, N = 183) and significantly shorter than E198K

276   and E420 mutant cells. Consistent with this observation, the E200K cells displayed a

277   significantly lower frequency of mitotic errors compared to E198K and E420K cells, the two

278   most severe mutations of the disease variants.

Discussion

279 **Discussion**

280   Our cryo-EM structures of the PP2A-B56δ holoenzyme, particularly in its closed form, reveal

281   distinct mechanisms by which it can exist in a dual latent state and become activated in response

282   to phosphorylation. The extended dynamic regulation interface of the holoenzyme provides a

283   coherent framework for understanding the holoenzyme's dual latency and activation, as well as

284   the shared mechanisms underlying the diverse disease mutations associated with neurological

285   disorders. The complexity of the holoenzyme regulation resides in the unprecedented length of

286   the regulation interface primarily formed by the intrinsically disordered regions rich in regulatory

287   elements. These elements include multiple phosphorylation sites on both N/C-arms, a cis-B56

288   SLiM and E574 on the C-arm, which establish dual autoinhibition in the closed form, and other

289   signaling sequences on the C-arm, such as nuclear localization signal (NLS) and SH3-binding

290   motif. In addition, the regulation interface is featured by multiple repulsive contacts that

291   contribute to its semi-stable and dynamic nature, which is responsive to phosphorylation and

292   disease mutations. Furthermore, REST2 MD simulation reveals an allosteric network closely

293   coupled to the regulation interface, reflecting the structural intricacy and coherency underlying

294   complex holoenzyme regulation.

295   The mutation spectrum in patients also corroborates our above notions on the regulation interface

296   in the B56δ holoenzyme. The latter, in turn, provides critical insights into the underlying

297   mechanisms of ID-associated disease mutations. Albeit the mutated residues of diverse variants

298   are widely separated spatially, the super-long regulation interface harbors nearly all of them like

299   an extended umbrella. The coupling of ID mutations to the regulation interface and the allosteric

300   network explains their shared symptoms, including intellectual disability, hypotonia, and

301   autism[8,9,12,13]. ID mutations at the holoenzyme regulation interface might perturb the holoenzyme

302   regulation and function in many scenarios, potentially leading to dominant negative effects. For

303   example, ID mutations might perturb the dual latency individually or simultaneously and alter

304   the activation phosphorylation rates of the holoenzyme. Furthermore, the loss of coherent dual

305   latency and perturbed holoenzyme activation might also lead to untimed exposure of NLS and

306   binding sites for SH3 and 14-3-3. Consistent with the latter notion, a family with B56δ missing

307   the C-arm showed incomplete penetrance of neurological disorders compared to other missense

308   variants that are *de novo* and completely penetrant[51]. The effects of B56δ mutations are also

309   supported by studies using CRISPR-edited HEK293 cells bearing heterozygotic or homozygotic

310 E420K[50]. This mutation in either single or both alleles perturbs the same diversity of signaling

311 nodes.

312 The involvement of the B56 SLiM and its binding groove at the regulation interface likely

313 contribute to the bulk of the broad range of clinical symptoms of Jordan Syndrome. The human

314 proteome has ~1,500 B56 SLiM-containing proteins involved in broad cellular signaling and

315 processes[17]. Perturbation of the dual latency and phosphorylation-induced holoenzyme activation

316 is expected to affect many of these B56 SLiM-containing signaling proteins. Consistently,

317 CRISPR-edited HEK293 cells bearing B56δ E420K altered 6% of phosphopeptides in the

318 proteome by at least 2-fold[50]. We showed that among ~1,000 genes in SFARI Gene database

319 with genes associated with autism and neurodevelopmental disorders (gene.sfari.org), >10%

320 possess B56-targeting SLiMs (data not shown), underlying overlapping molecular processes

321 perturbed by Jordan Syndrome and SFARI genes. In addition to the effects of ID mutations on

322 mitosis (Fig. 6), the E420K mutation was shown to affect mTOR/AKT signaling among other

323 signaling processes[50]. Coupling to PP2A holoenzyme SLiMs is an emerging theme of signaling

324 and functional complexity. For example, the multiple PP2A holoenzyme SLiMs in the PP2A

325 methylesterase (PME-1) creates versatile PME-1 activities toward PP2A holoenzymes, diverse

326 signaling pathways, and cellular processes[31].

327 In addition to the shared mechanisms across variants, our study begins to illuminate the

328 molecular basis of the genotype-phenotype correlation of clinical severity. Clinical studies

329 showed that E198K is the most severe form of the disease and that E420K is more severe than

330 the E200K and E197K variants[8,9,12]. We showed that the E198K holoenzyme has a much higher

331 basal level of substrate SLiM-binding than the WT holoenzyme and other disease variants (Fig.

332 5e). Furthermore, E198K and E420K cause longer mitotic duration than WT and E200K and

333   gave higher mitotic error rates than the E200K variant (Fig. 6). In a companion paper focusing

334   on the changes of the holoenzyme allosteric paths by E198K and E200K, we showed that the

335   E198K holoenzyme has an allosteric pathway resembling the holoenzyme with activation

336   phosphorylation, underlying a higher basal activity and loss of latency of this variant[52]. In

337   contrast, the allosteric pathway is minimally affected by E200K. Many questions remain to be

338   answered. Our study laid the critical foundation for understanding the function and regulation of

339   the B56δ holoenzyme and an in-depth understanding of the underlying mechanisms of Jordan

340   Syndrome mutations.

341   It is important to stress the super-dynamic nature of the regulation interface formed by the

342   disordered N/C-arms and the holoenzyme core. Our challenges to capture the closed form of the

343   WT holoenzyme by single-particle cryo-EM suggests the presence of many conformation states

344   that might be required for numerous nuances of cellular signaling under normal physiological

345   conditions. Two distinct structural features might contribute to the super-dynamic nature: the

346   interactions of two extended intrinsically disordered regions from the widely separated N/C-arms

347   and the multiple repulsive contacts along the interface. Enriching broad regulation elements in

348   the disordered regions forms one more basis for the complexity and intricacy of this regulation

349   interface. The structural and functional features outlined here might not be unique to the B56δ

350   holoenzyme but are a common theme for modulating complex biological processes and signaling

351   that remain to be broadly studied.

Author Contributions

353   CGW performed cryo-EM studies, assisted and guided by HW, BC, WKC, and YX. CGW and

354   YX determined the structures. CGW, VKB, and PSP performed biochemical studies, assisted by

355 RS. KK performed REST2 simulation, guided by XH and YX. BEW generated anti-pS573

356 antibody. MS, AM generated CRISPR cell lines, guided by RH. YCC, CGW, and RS performed

357 cell biology, guided by YX and AS. RAM developed and tested the holoenzyme sensor, guided

358 by SS. YX performed data analysis and structural analysis, developed the figure panels, and

359 wrote the manuscript, assisted by CGW.

Acknowledgement

372

Materials and Methods

Protein preparation

All protein constructs were generated by standard PCR molecular cloning strategy. The human His$_6$-tagged scaffold A-subunit (α isoform), His$_8$-tagged PP2Ac (α isoform), and GST-tagged B56δ were overexpressed in insect cells using the lab-modified Bac-to-Bac baculovirus expression system[53,54]. Briefly, Hi-5 cells grown to a density of 1.5×10^6 cell/ml were co-infected with PP2A His-scaffold A subunit, His-PP2Ac, and GST-B56δ baculovirus for 48h at 27ºC. Cells were lysed by Dounce homogenization in the lysis buffer containing 25mM Tris-HCl (pH 8.0), 150mM NaCl, 50 μM MnCl$_2$, 2mM DTT, and protease inhibitors (10μM leupeptin, 0.5 μM Aprotinin and 1mM PMSF). The insoluble proteins were removed by centrifugation, and the soluble fraction of cell lysates was gravity-loaded to GS4B (Glutathione Sepharose 4B) resin (Cytiva) column three times followed by two washes using 5 column volumes (CV) of lysis buffer. The proteins left on the resins were digested by the TEV protease, and the flow-through was further fractionated by anion exchange chromatography (Source 15Q column, Cytiva) and gel filtration chromatography (Superdex 200 column, Cytiva). The point mutations for the B56δ disease variants and/or truncations of the B56δ N/C-arms were introduced by site-directed mutagenesis, and the mutant and/or truncated holoenzymes were expressed and purified similarly to the WT holoenzyme. GST-tagged SYT16 (132-147) and CREB (99-161) were overexpressed in *E. coli* DH5α and purified over GS4B resin and ion exchange chromatography.

GST-mediated pulldown assay

To test the interaction between WT and mutant PP2A-B56δ holoenzyme with substrate B56 SLiM peptides, 12 μg of GST-tagged SYT16 (132-147) or GST-tagged CREB (99-161) was

395   immobilized on 5 µl of GS4B resin. The unbound protein was washed out by assay buffer

396   containing 25 mM Tris (pH 8.0), 150 mM NaCl, 3 mM DTT, and 1x protease inhibitor cocktail

397   (P8340, Sigma). 10 µM of PP2A-B56δ holoenzymes were then added to the immobilized GST-

398   tagged protein in a final volume of 50 µl assay buffer supplemented with 1mg ml^{-1} of BSA. After

399   5 min of incubation, the unbound proteins were removed, and the resins were washed three times

400   with the assay buffer supplemented with 0.1% of Triton X-100. The proteins that remained on

401   the resin were examined by SDS-PAGE and visualized by Coomassie blue staining.

402   **Cross-linking mass spectrometry (XL-MS) of the PP2A-B56δ holoenzyme**

403   The intra-molecular interactions in the PP2A-B56δ holoenzyme were probed by EDC zero-

404   length chemical crosslinker, followed by mass spectrometry analysis. In brief, 1.5 µM PP2A-

405   B56δ holoenzyme in 25 mM MES (pH6.0) and 150 mM NaCl was incubated with 60 mM EDC

406   at RT for 75 min, followed by quenching the reaction with 100 mM Tris. The crosslinked

407   samples were desalted by desalting columns (Zepa spin desalting column, Thermo Fisher

408   Scientific) and analyzed by SDS-PAGE. The bands representing holoenzymes with inter-subunit

409   crosslinks were excised from SDS-PAGE for reduction and in-gel digestion. The excised bands

410   were reduced in 25mM DTT and 25mM NH$_4$HCO$_3$ at 57ºC for 30 min and alkylated with 55mM

411   IAA in 25 mM NH$_4$HCO$_3$ in darkness for 30 min at RT, followed by digestion in 20 µl of 10ng

412   ul^{-1} Trypsin (Promega) in 25 mM NH4HCO3 (pH 8.0-8.5) and 0.01% ProteaseMAX w/v

413   (Promega) for 16 hr at 37ºC. To improve peptide detection and sequence coverage, secondary

414   digestion was performed with 20ng µl^{-1} GluC or chymotrypsin in 25 mM NH$_4$HCO$_3$ for 8 hr at

415   37ºC and quenched by 0.05% TFA, followed by desalting with C18 cartridges. The resulting

416   samples were then separated and analyzed by LC-MS/MS using Lumos mass spectrometer. The

417   identification of peptides for all three subunits was conducted by MeroX software[55]. Multiple

418   XL-MS experiments were performed, and four with 90% sequence coverage were used to

419   identify crosslinked residue pairs. The detection frequency for reliable residue pairs was

420   evaluated using the identical pairs in the crystal structure of the PP2A-B56γ1 holoenzyme (PDB:

421   2NPP).

422   **Cryo-EM sample preparation and data acquisition**

423   The cryo-EM grids for the WT PP2A-B56δ holoenzyme were prepared at the New York

424   Structural Biology Center using a prototype of the commercial Chameleon system (SPT Labtech)

425   based on the Spotiton technology[45,46]. 50 pl of the WT holoenzyme at a concentration of 1.6

426   mg ml^{-1} was applied to the homemade self-wicking nanowire grids[56] using a piezo-electric

427   dispenser, followed by plunge-frozen in liquid ethane. The robot chamber was operated at room

428   temperature without strictly controlled but moderate humidity. The cryo-EM data for the WT

429   holoenzyme was collected using Titan Krios (ThermoFisher) electron microscope operated at

430   300 kV equipped with Gatan K2 summit cameras. A total of 1790 movies were automatically

431   acquired by Leginon[57] with a defocus range of -1.2 to -2μm at a nominal magnification of

432   105,000×, corresponding to a pixel size of 1.096 Å/pixel. Each stack dose-fractioned over 50

433   frames was recorded with a total electron dose of 66.84 eÅ^{-2}.

434   For the E197K PP2A-B56δ holoenzyme, an aliquot of 3 μl of purified holoenzyme at 0.4 mg ml^{-}

435   ^{1} was applied onto a glow-discharged holey gold grids (UltraAuFoil R1.2/1.3), blotted for 4 s

436   with a blot force of -5 and plunge frozen in liquid ethane using a FEI Vitrobot Mark IV (Thermo

437   Fisher Scientific) at 4℃ and 100% humidity. Cryo-EM data were collected using a Titan Krios

438   operating at 300 kV with a Gatan K3 detector and GIF Quantum energy filter. A total of 9158

439   movies were collected using SerialEM, with a slit width of 20 eV on the energy filter and a

440   defocus range from -0.7 to -2.2 μm in super-resolution counting mode at a nominal

441 magnification of 81,000×, corresponding to a pixel size of 1.068 Å/pixel. Each stack dose-

442 fractioned 69 frames was recorded for a total exposure time of 3.2 s and electron dose of 49

443 eÅ^{-2}.

Cryo-EM data processing

445 All data were processed with similar strategies and procedures using cryoSPARC 3.0[58]. Movies

446 were motion-corrected using Patch Motion Correction, followed by the contrast transfer function

447 (CTF) estimation using Patch CTF Estimation. Images with bad CTF estimations worse than 4Å

448 were discarded. Particles were first picked from thirty good images using Blob Picker and

449 extracted with a box size of 280Å. Good 2D class averages showing projections in different

450 orientations were selected as templates for automatic picking for the entire dataset. Reiterate 2D

451 classification was used to remove bad particles. The remaining good particles were used for ab

452 initio reconstruction, followed by heterogeneous and homogenous refinements, with particles

453 from bad classes removed in each reiterate procedure. Different conformations of the PP2A-

454 B56δ holoenzyme were best separated by 3D variability analysis (3DVA)[59]. Particles from

455 conformationally homogeneous classes were then subjected to homogenous refinement, followed

456 by local and global CTF refinement. Local refinement with a mask around the close

457 conformation of the B56δ subunit was performed to obtain a better resolution for this subunit.

458 These efforts gave maps with a resolution of 3.13 Å for the loose form and 2.59 Å for the closed

459 form of the E197K PP2A-B56δ holoenzyme. The resolution was estimated by applying a soft

460 mask around the protein complex and using the gold-standard Fourier shell correlation (FSC) =

461 0.143 criterion.

Model building and refinement

463   The initial model of the PP2A-B56δ complex was built on the structure of PP2A-B56γ1

464   holoenzyme (PDB ID: 2NPP) and manually docked into the cryo-EM maps in Chimera[60].

465   Modifications to the holoenzyme core and model building of the N/C-arms were performed in

466   COOT[61]. The structural model was refined using the phenix.real_space_refine program in

467   PHENIX[62] with secondary structure and geometry restraints. The final models were analyzed

468   using MolProbity[63].

469   **Phosphatase assay**

470   The enzyme kinetics of the purified PP2A-B56δ holoenzymes were determined using the

471   PiColorLock phosphatase assay (Abcam, Ab270004), measuring the release of inorganic

472   phosphate from the dephosphorylation of substrates. A phosphorylated hexapeptide (KRpTIRR)

473   was used as the substrate for the assay. 50ul of 30nM indicated PP2A-B56δ holoenzymes in the

474   assay buffer, containing 25mM Tris pH8.0, 150mM NaCl, and 50uM $MnCl_2$ supplemented with

475   0.05 mg ml-1 BSA, were added to the 10μl substrate (6 times of the final concentration prepared

476   in the assay buffer) in a 96-well clear plate to start the reactions. After 3 min, the reactions were

477   quenched by 15 μl of quench buffer provided in the kit and allowed the color to develop for 15

478   min. The absorbance at 635nm of the reactions was then read by the SpectraMax Plus

479   384 Microplate Reader (Molecular Devices) using the end-point mode. Initial velocity (V_0)

480   determined at varying concentrations of substrate was calculated and fit to the Michaelis–Menten

481   equation (eq. 1) to determine the steady-state kinetics of the PP2A-B56 holoenzymes.

482   (1) $$v = \frac{k_{cat}[E][S]}{K_m + [S]}$$

483

484   In eq. 1, kcat is the rate constant, [E] and [S] are the enzyme and substrate concentration, and

485   Km is the Michaelis-Menten constant reflecting the binding affinity between the peptide

486   substrate and the enzyme.

487   ***In vitro* holoenzyme phosphorylation by protein kinase A (PKA)**

488   100 μl PP2A-B56δ holoenzyme was prepared to a final concentration at 0.1mg ml^{-1} in assay

489   buffer containing 50 mM Tris-HCl (pH7.5), 10 mM $MgCl_2$, 200 uM ATP, 0.1 mM EDTA, 2 mM

490   DDT, and 0.01% Brij35. Phosphorylation was initiated by adding 1 μl PKA at 0.1mg ml^{-1} to the

491   PP2A-B56δ holoenzymes (PKA: PP2A-B56δ = 1: 100 (w/w)) and incubating the mixture at

492   37°C. 10 μl PP2A-B56 holoenzyme was taken out at the indicated time from the reaction, mixed

493   with 3 μl of 4x SDS dye (40% Glycerol, 8% SDS, 0.25M Tris-HCL, pH 6.8,0.4M DTT,0.04%

494   bromophenol blue) and immediately heated at 95°C for 3 min to quench the reaction. 0.05 μg of

495   PP2A-B56 holoenzyme from each time point were examined by western blot. To detect the

496   phosphorylation level at S573 of B56δ, we utilized a newly developed antibody that recognizes

497   pS573 (see supplemental information). The total B56δ was detected by a commercial antibody

498   (Invitrogen, MA-26636).

499   **Mammalian cell culture and the time course of B56δ phosphorylation upon cellular cAMP**

500   **activation**

501   Human embryonic kidney cells (HEK293T) cells were cultured in Dulbecco's modified Eagle's

502   medium (Gibco, Thermo Fisher Scientific, Waltham, MA, USA) with 10% fetal bovine serum

503   (Hyclone, GE Healthcare, Boston, MA, USA), 100 U ml^{-1} penicillin, and 100 μg ml^{-1}

504   streptomycin in a humidified atmosphere at 37 °C with 5% CO2.

505   Following transit transfection of the Flag-tagged B56δ (WT, E198K, E200K, and E420K), the

506   HEK293T cells were treated with 10uM forskolin (Fsk; Sigma: 344270-10MG) and 1mM

507   isobutylmethyxanthine (IBMX; Cayman:13347) to stimulate cellular cAMP/PKA. The cells were

508   harvested at the indicated time following stimulation and lysed using a buffer containing 20mM

509   Tris-HCl pH7.0, 150mM NaCl, 0.1% Triton X-100, 10uM H89 (PKA inhibitor), 10ug ml^{-1}

510   DNase, protease inhibitor and phosphatase inhibitor (phoSTOP, Sigma-Millipore). Total cell

511   lysates (20 μg) for each time point were examined by Western blot using antibody that

512   specifically recognizes pS573. The levels of pS573 were normalized to the total B56δ detected

513   by a specific antibody (Invitrogen-Thermal Scientific, MA-26636). At least six experimental

514   repeats were performed to determine the fluctuation range of the activation phosphorylation

515   rates. The P-values for the time-dependent increase of pS573 were calculated using Jonckheere-

516   Terpstra test in MSTAT7.0 (https://oncology.wisc.edu/mstat/).

517   **REST2 simulation**

518   The cryo-EM structure of the closed form of the E197K PP2A-B56δ holoenzyme was used to

519   generate the initial model for the close forms of WT, E198K, and E200K holoenzymes.

520   Molecular dynamics (MD) simulations were performed using Gromacs[64] patched with

521   PLUMED 2.8.0 in the Amber ff14SB forcefield[65]. The protonation state of protein residues was

522   determined by propka 3.4.0. The short-range Coulomb interactions were cut off at 0.9 nm, and

523   long-range electrostatics were computed with PME (particle-mesh Ewald). The Lennard-Jones

524   interactions were cut off at 0.9 nm. The structure was simulated in a dodecahedron box, with the

525   minimum distance to the surface of the protein of 1 nm. The complex was solvated in TIP3P

526   water (approximately 60,000 water molecules), and sodium ions were added until the system was

527   neutral. The energy of the system was minimized with the steepest descent algorithm for 10,000

528   steps. Then, 1 ns MD simulations were performed at 310K with the positions of all protein atoms

529   except hydrogen restrained. In these simulations, the temperature was controlled by a V-rescale

530   thermostat with a coupling constant of 10 ps, and pressure set to 1 bar controlled by a C-rescale

531   barostat with a coupling constant of 1 ps. Snapshots used for analysis were spaced by 100 ps.

532   Conventional MD simulations are not successful in sampling the dissociations of the N/C-arms.

533   We thus have adopted an enhanced sampling technique: REST2[49], with the terminal 8 residues of

534   the N/C-arms placed in a "hot region". 20 independent replicas were run with the "hot region"

535   temperatures assigned to a geometric progression: 310, 320, 332, 344, 356, 368, 381, 395, 409,

536   423, 438, 454, 470, 486, 503, 521, 540, 559, 578, and 600K. Exchanges between replicas were

537   attempted every 500 steps and the acceptance probability achieved was ~20%. REST2

538   simulations were conducted up to 100 ns, totaling 2µs of simulation time per PP2A variant.

539   **Allosteric network**

540   The allosteric networks were computed for each variant of the PP2A using an established graph-

541   theoretic approach[66,67]. To compute a network, each residue in the holoenzyme was represented

542   by two atoms: Cα and the non-hydrogen sidechain atom most distant from the Cα. For residues

543   Ala, Gly and Pro only the Cα atom was used. Then, using all the conformations from the REST2

544   simulations at T=310K, linear mutual information (LMI) C_{ij} between all pairs of atoms was

545   computed using g_correlation[68]. Next, the resulting LMI matrix was multiplied with a semi-

546   binary contact map, so that only the neighboring atoms would have a significant contribution to

547   the network. The contact map K between each pair of selected atoms is a piecewise smoothing

548   function as used by Botello-Smith *et al*[69]:

$$K(r) = \begin{cases} 1 \text{ if } r \leq r_{full} \\ \dfrac{e^{-\frac{r^2}{2\sigma^2}}}{e^{-\frac{r_{full}^2}{2\sigma^2}}} \text{ if } r > r_{full} \end{cases}$$

549   Where r is the distance between the selected atoms in an MD snapshot. The cutoff distance for a

550   full contact was selected as $r_{full} = 0.8$ nm and $r_{cut} = 1.5\ nm$, so $K(r_{cut} = 1.5) = 10^{-5}$ and

551    $\sigma = \sqrt{\dfrac{r_{full}^2 - r_{cut}^2}{2 \ln K(r_{cut})}} \approx 0.264$. Then, $m_{ij} = \dfrac{1}{N_{frames}} \sum_{n=1}^{N_{frames}} K\left(r_{ij}(n)\right)$ are the elements of the

552   contact map averaged over all frames in the simulation. The LMI matrix with a contact cutoff

553   was used to define the network, where the selected atoms served as nodes, and the edges were

554   equal to the masked LMI. The edge weights in the network were computed as $w_{ij} = -log|L_{ij}|$

555   where $L_{ij} = m_{ij}\ C_{ij}$. Paths in this network weighed by the edges explain how strongly the

556   correlated motion of residues in the source affects residues in the sink and were computed with

557   the Dijkstra algorithm using the "networkX" python library (*https://networkx.github.io* (2020)).

558   Finally, the number of times a residue was crossed by the shortest paths was counted, and

559   contribution from individual atoms in the residue were summed up. This count, normalized by

560   the maximum count in the network, was used as the weight of the residue in the overall allosteric

561   network. Confidence intervals were computed as the standard deviation of residue weight in

562   networks obtained from 10 bootstrapped trajectories. The bootstrapped trajectories of 100 ns

563   were obtained by selecting blocks of 10 ns from the original dataset with replacement.

564   **Mammalian cell holoenzyme sensor to detect conformation transition upon activation**

565   N-terminal large (LgBit) and C-terminal small (SmBit) fragments derived from NanoLuc

566   (Promega) were fused to the C-terminus of B56δ and inserted downstream of its N-arm at

567   residue 103, respectively. The SmBit sequence is sandwiched by a short linker sequence, "GSG"

568   at both ends to alleviate structural hindrance for complementation with LgBit. The constructs

569   expressing the B56δ holoenzyme conformation sensors were transfected into COS-1 cells. After

570   24 hours, cells were placed in 20% Nano-Glo® Live Cell Reagent (Promega) mixed with 80%

571   DMEM containing 1% FBS. Cells were equilibrated at 37 °C in 5% CO_2 in a Cytation 5 before

572   the luminescence readings were measured every 5 minutes. Following the second reading, cells

573   were treated with 20 μM forskolin (Tocris) and 2 μM rolipram (Tocris) to activate adenylyl

574   cyclase and inhibit cAMP phosphodiesterase 4 (PDE4) simultaneously to activate cellular

575   cAMP/PKA. All values were normalized to the vehicle control, and all wells were normalized to

576   the 5-min time point (just before forskolin/rolipram treatment). The experiments were performed

577   in quadruplicate and repeated three times. Representative results were shown. Error bars

578   represent standard deviation.

579   **CRISPR prime editing to introduce B56δ ID mutations**

580   A single genomic change of ID mutations was introduced into HEK-293 cells to one or both

581   alleles of *PPP2R5D*. The CRISPR knock-in of the E420K B56δ mutation was produced by

582   cytidine base editing of the coding sequence in exon 12 of *PPP2R5D* as previously described[50].

583   The heterozygotic and homozygotic E198K knock-ins and the heterozygotic E200K knock-in

584   were produced by prime editing PE3b strategy[70]. Briefly, Cas9 nickase fused to an engineered

585   reverse transcriptase (RT) with improved thermostability and processivity (PE2) was

586   programmed with a prime editing guide RNA (pegRNA) to nick and edit the PAM strand. Once

587   the DNA strap on the edited strand was resolved, a secondary single guide RNA (sgRNA) that

588   matches only the edited strand, not the original allele, guided the Cas9 domain of PE2 to nick the

589   non-edited strand. This strategy, known as PE3b[70], improved editing efficiency without

590   introducing double-strand breaks and reduced off-target edits. The pCMV-PE2 plasmid

591   expressing PE2 Cas9-RT fusion protein (Addgene plasmid #132775,

592   https:www.addgene.org/132775/) was provided as a generous gift from Dr. David Liu. For each

593   knock-in mutation, a dual RNA expression cassette containing sequences encoding a mutation-

594   specific pegRNA (driven by an hU6 promoter) targeting *PPP2R5D* exon 5, and the secondary

595   mutation-specific sgRNA (driven by a 7SK promoter) was synthesized and cloned into pUC57-

596   kan vector.

597   Approximately 200,000 wild-type HEK-293 cells were electroporated with pCMV-PE2 and the

598   appropriate RNA expression plasmid using a Neon transfection system for each knock-in

599   mutation. After 48h of recovery, electroporated cells were clonally isolated by single-cell sorting

600   into 96 well plates using a BD FACS Aria II. After clonal expansion, genomic DNA was

601   isolated, and regions containing exon 5 were PCR-amplified. Sanger sequencing was then

602   employed to detect the desired single-base mutations. Before further use, cell lines with the

603   desired mutations were single-cell sorted three times to ensure each cell line represents a

604   homogenous population derived from a single gene-edited cell. Complete genomic sequencing of

605   the parental, E420K, E200K, and E198K variant cell lines was performed to characterize the

606   genomic background, detect any off-target editing, and ensure that repetitive single-cell sorting

607   did not introduce spontaneous somatic mutations. Cell lines with off-target mutations detected in

608   protein-coding regions were discarded. Details for the E198K prime edited cell lines are

609   described elsewhere[71]. The design of pegRNAs and sgRNAs for E200K is described in

610   supplemental materials.

611   **Live cell imaging and mitotic duration measurements**

612   To investigate whether the B56δ ID mutation, E198K, E200K, or E420K affects the mitotic

613   duration and fidelity, we used high temporal resolution live-cell imaging to monitor the mitotic

614   progression of HEK293T cells with the WT B56δ or CRISPR knock-in ID mutation. Nikon Ti-E

615   inverted microscope equipped with a Photometrics CoolSnap Hq2 CCD camera, spectra-X LED

616   light source (Lumencor), and a Plan Apo 20x objective (NA = 0.45) controlled by Nikon

617   Element software was used for live imaging. Time-lapse imaging collected 5 frame 3D stacks at

618   2 μm steps along the z-axis at 3 min intervals for 24-48 hours. All cells were grown on a 4-

619   chambered glass bottom dish (#1.5 glass, Cellvis) in FluoroBrite DMEM media (Thermo Fisher)

620   supplemented 10% FBS (Gibco) and 2 mM GlutaMAX (Gibco). All cells were incubated with

621   sirDNA and 10 μM of verapamil (Cytoskeleton, Inc.) for 4 hours before live imaging. Cells were

622   recorded at 37°C with 5% CO_2 in a stage-top incubator using the feedback control to maintain

623   the growing media's temperature (Tokai Hit, STX model). Image analysis was performed using

624   Nikon Element software. Mitotic stages were determined by nuclear staining. The mitotic

625   duration was measured from nuclear envelope breakdown (NEBD) to anaphase onset. Incidences

626   of lagging chromosomes were analyzed. The experiments were independently repeated three

627   times, and P-values between variants were calculated by One-Way Anova and two-tailed t-test.

628   P-values < 0.05 were considered significant.

629

References

1. Arnold, H.K. & Sears, R.C. A tumor suppressor role for PP2A-B56α through negative regulation of c-Myc and other key oncoproteins. *Cancer and Metastasis Reviews* **27**, 147-158 (2008).
2. Wlodarchak, N. & Xing, Y. PP2A as a master regulator of the cell cycle. *Crit Rev Biochem Mol Biol* **51**, 162-84 (2016).
3. Virshup, D.M. Protein phosphatase 2A: a panoply of enzymes. *Curr Opin Cell Biol* **12**, 180-5 (2000).
4. Strack, S. et al. Protein phosphatase 2A holoenzyme assembly: identification of contacts between B-family regulatory and scaffolding A subunits. *J Biol Chem* **277**, 20750-5 (2002).
5. Saraf, A., Oberg, E.A. & Strack, S. Molecular determinants for PP2A substrate specificity: charged residues mediate dephosphorylation of tyrosine hydroxylase by the PP2A/B′ regulatory subunit. *Biochemistry* **49**, 986-995 (2010).
6. Shi, Y. Serine/threonine phosphatases: mechanism through structure. *Cell* **139**, 468-84 (2009).
7. Study., D.D.D. Prevalence and architecture of de novo mutations in developmental disorders. *Nature* **542**, 433-438 (2017).
8. Shang, L. et al. De novo missense variants in PPP2R5D are associated with intellectual disability, macrocephaly, hypotonia, and autism. *Neurogenetics* **17**, 43-9 (2016).
9. Houge, G. et al. B56delta-related protein phosphatase 2A dysfunction identified in patients with intellectual disability. *J Clin Invest* **125**, 3051-62 (2015).
10. Cerami, E. et al. The cBio cancer genomics portal: an open platform for exploring multidimensional cancer genomics data. *Cancer Discov* **2**, 401-4 (2012).
11. Gao, J. et al. Integrative analysis of complex cancer genomics and clinical profiles using the cBioPortal. *Sci Signal* **6**, pl1 (2013).
12. Biswas, D., Cary, W. & Nolta, J.A. PPP2R5D-Related Intellectual Disability and Neurodevelopmental Delay: A Review of the Current Understanding of the Genetics and Biochemical Basis of the Disorder. *Int J Mol Sci* **21**(2020).
13. Oyama, N. et al. Clinical, neuroimaging and molecular characteristics of PPP2R5D-related neurodevelopmental disorders: an expanded series with functional characterisation and genotype-phenotype analysis. *J Med Genet* (2022).
14. Walker, I.M. et al. PPP2R5D Genetic Mutations and Early-Onset Parkinsonism. *Ann Neurol* **89**, 194-195 (2021).
15. Hetzelt, K. et al. Early-onset parkinsonism in PPP2R5D-related neurodevelopmental disorder. *Eur J Med Genet* **64**, 104123 (2021).
16. Kim, C.Y. et al. Early-Onset Parkinsonism Is a Manifestation of the PPP2R5D p.E200K Mutation. *Ann Neurol* **88**, 1028-1033 (2020).
17. Wu, C.G. et al. PP2A-B' holoenzyme substrate recognition, regulation and role in cytokinesis. *Cell Discov* **3**, 17027 (2017).
18. Hertz, E.P. et al. A Conserved Motif Provides Binding Specificity to the PP2A-B56 Phosphatase. *Mol Cell* **63**, 686-95 (2016).
19. Wang, J. et al. Crystal structure of a PP2A B56-BubR1 complex and its implications for PP2A substrate recruitment and localization. *Protein & cell* **7**, 516-526 (2016).
20. Davey, N.E. & Morgan, D.O. Building a regulatory network with short linear sequence motifs: lessons from the degrons of the anaphase-promoting complex. *Molecular cell* **64**, 12-23 (2016).

21. Davey, N.E., Cyert, M.S. & Moses, A.M. Short linear motifs–ex nihilo evolution of protein regulation. *Cell Communication and Signaling* **13**, 43 (2015).

22. Wigington, C.P. et al. Systematic discovery of Short Linear Motifs decodes calcineurin phosphatase signaling. *Molecular Cell* **79**, 342-358. e12 (2020).

23. Ueki, Y. et al. A consensus binding motif for the PP4 protein phosphatase. *Molecular Cell* **76**, 953-964. e6 (2019).

24. Heroes, E. et al. The PP1 binding code: a molecular-lego strategy that governs specificity. *The FEBS journal* **280**, 584-595 (2013).

25. Nasa, I., Rusin, S.F., Kettenbach, A.N. & Moorhead, G.B. Aurora B opposes PP1 function in mitosis by phosphorylating the conserved PP1-binding RVxF motif in PP1 regulatory proteins. *Science signaling* **11**(2018).

26. Wang, X., Bajaj, R., Bollen, M., Peti, W. & Page, R. Expanding the PP2A Interactome by Defining a B56-Specific SLiM. *Structure* **24**, 2174-2181 (2016).

27. Kruse, T. et al. Direct binding between BubR1 and B56-PP2A phosphatase complexes regulate mitotic progression. *J Cell Sci* **126**, 1086-92 (2013).

28. Bastos, R.N., Cundell, M.J. & Barr, F.A. KIF4A and PP2A-B56 form a spatially restricted feedback loop opposing Aurora B at the anaphase central spindle. *J Cell Biol* **207**, 683-93 (2014).

29. Ueki, Y. et al. A highly conserved pocket on PP2A-B56 is required for hSgo1 binding and cohesion protection during mitosis. *EMBO Rep* **22**, e52295 (2021).

30. Ito, A. et al. A truncated isoform of the PP2A B56 subunit promotes cell motility through paxillin phosphorylation. *Embo J* **19**, 562-71 (2000).

31. Li, Y. et al. Coupling to short linear motifs creates versatile PME-1 activities in PP2A holoenzyme demethylation and inhibition. *Elife* **11**(2022).

32. Ambjorn, S.M. et al. A complex of BRCA2 and PP2A-B56 is required for DNA repair by homologous recombination. *Nat Commun* **12**, 5748 (2021).

33. Kim, S.H., Wu, C.G., Jia, W., Xing, Y. & Tibbetts, R.S. Roles of constitutive and signal-dependent protein phosphatase 2A docking motifs in burst attenuation of the cyclic AMP response element-binding protein. *J Biol Chem* **297**, 100908 (2021).

34. Lambrecht, C. et al. Loss of protein phosphatase 2A regulatory subunit B56delta promotes spontaneous tumorigenesis in vivo. *Oncogene* **37**, 544-552 (2018).

35. Liu, L. & Eisenman, R.N. Regulation of c-Myc Protein Abundance by a Protein Phosphatase 2A-Glycogen Synthase Kinase 3beta-Negative Feedback Pathway. *Genes Cancer* **3**, 23-36 (2012).

36. Arnold, H.K. et al. The Axin1 scaffold protein promotes formation of a degradation complex for c-Myc. *Embo J* **28**, 500-12 (2009).

37. Arnold, H.K. & Sears, R.C. A tumor suppressor role for PP2A-B56alpha through negative regulation of c-Myc and other key oncoproteins. *Cancer Metastasis Rev* **27**, 147-58 (2008).

38. Arnold, H.K. & Sears, R.C. Protein phosphatase 2A regulatory subunit B56alpha associates with c-myc and negatively regulates c-myc accumulation. *Mol Cell Biol* **26**, 2832-44 (2006).

39. Dodge-Kafka, K.L. et al. cAMP-stimulated protein phosphatase 2A activity associated with muscle A kinase-anchoring protein (mAKAP) signaling complexes inhibits the phosphorylation and activity of the cAMP-specific phosphodiesterase PDE4D3. *J Biol Chem* **285**, 11078-86 (2010).

40. Ahn, J.H. et al. Protein kinase A activates protein phosphatase 2A by phosphorylation of

the B56delta subunit. *Proc Natl Acad Sci U S A* **104**, 2979-84 (2007).

41. Flynn, M.P. et al. Luteinizing hormone receptor activation in ovarian granulosa cells promotes protein kinase A-dependent dephosphorylation of microtubule-associated protein 2D. *Mol Endocrinol* **22**, 1695-710 (2008).

42. Margolis, S.S. et al. Role for the PP2A/B56delta phosphatase in regulating 14-3-3 release from Cdc25 to control mitosis. *Cell* **127**, 759-73 (2006).

43. Forester, C.M., Maddox, J., Louis, J.V., Goris, J. & Virshup, D.M. Control of mitotic exit by PP2A regulation of Cdc25C and Cdk1. *Proc Natl Acad Sci U S A* **104**, 19867-72 (2007).

44. Shouse, G.P., Nobumori, Y., Panowicz, M.J. & Liu, X. ATM-mediated phosphorylation activates the tumor-suppressive function of B56gamma-PP2A. *Oncogene* **30**, 3755-65 (2011).

45. Levitz, T.S., Brignole, E.J., Fong, I., Darrow, M.C. & Drennan, C.L. Effects of chameleon dispense-to-plunge speed on particle concentration, complex formation, and final resolution: A case study using the Neisseria gonorrhoeae ribonucleotide reductase inactive complex. *J Struct Biol* **214**, 107825 (2022).

46. Jain, T., Sheehan, P., Crum, J., Carragher, B. & Potter, C.S. Spotiton: a prototype for an integrated inkjet dispense and vitrification system for cryo-TEM. *J Struct Biol* **179**, 68-75 (2012).

47. Xu, Y. et al. Structure of the protein phosphatase 2A holoenzyme. *Cell* **127**, 1239-51 (2006).

48. Cho, U.S. & Xu, W. Crystal structure of a protein phosphatase 2A heterotrimeric holoenzyme. *Nature* **445**, 53-7 (2007).

49. Wang, L., Friesner, R.A. & Berne, B.J. Replica exchange with solute scaling: a more efficient version of replica exchange with solute tempering (REST2). *J Phys Chem B* **115**, 9431-8 (2011).

50. Papke, C.M. et al. A disorder-related variant (E420K) of a PP2A-regulatory subunit (PPP2R5D) causes constitutively active AKT-mTOR signaling and uncoordinated cell growth. *J Biol Chem* **296**, 100313 (2021).

51. Liu, R. et al. A novel nonsense mutation in PPP2R5D is associated with neurodevelopmental disorders and shows incomplete penetrance in a Chinese pedigree. *Clin Neurol Neurosurg* **223**, 107524 (2022).

52. Disease Mutations and Phosphorylation Alter the Allosteric Pathways Involved in Autoinhibition of Protein Phosphatase 2A. (2023).

53. Stanevich, V. et al. The Structural Basis for Tight Control of PP2A Methylation and Function by LCMT-1. *Mol Cell* **41**, 331-42 (2011).

54. Zhang, L. et al. Eya3 partners with PP2A to induce c-Myc stabilization and tumor progression. *Nat Commun.* **9**, 1047. doi: 10.1038/s41467-018-03327-4. (2018).

55. Iacobucci, C. et al. A cross-linking/mass spectrometry workflow based on MS-cleavable cross-linkers and the MeroX software for studying protein structures and protein-protein interactions. *Nat Protoc* **13**, 2864-2889 (2018).

56. Wei, H. et al. Optimizing "self-wicking" nanowire grids. *J Struct Biol* **202**, 170-174 (2018).

57. Suloway, C. et al. Automated molecular microscopy: the new Leginon system. *J Struct Biol* **151**, 41-60 (2005).

58. Punjani, A., Rubinstein, J.L., Fleet, D.J. & Brubaker, M.A. cryoSPARC: algorithms for rapid unsupervised cryo-EM structure determination. *Nat Methods* **14**, 290-296 (2017).

59. Punjani, A. & Fleet, D.J. 3D variability analysis: Resolving continuous flexibility and discrete heterogeneity from single particle cryo-EM. *J Struct Biol* **213**, 107702 (2021).

768 60. Pettersen, E.F. et al. UCSF Chimera--a visualization system for exploratory research and
769   analysis. *J Comput Chem* **25**, 1605-12 (2004).
770 61. Emsley, P., Lohkamp, B., Scott, W.G. & Cowtan, K. Features and development of Coot.
771   *Acta Crystallographica Section D: Biological Crystallography* **66**, 486-501 (2010).
772 62. Adams, P.D. et al. PHENIX: a comprehensive Python-based system for macromolecular
773   structure solution. *Acta Crystallographica Section D: Biological Crystallography* **66**, 213-
774   221 (2010).
775 63. Chen, V.B. et al. MolProbity: all-atom structure validation for macromolecular
776   crystallography. *Acta Crystallographica Section D: Biological Crystallography* **66**, 12-21
777   (2010).
778 64. Hess, B., Kutzner, C., van der Spoel, D. & Lindahl, E. Gromacs 4: algorithms for highly
779   efficient, load-balanced, and scalable molecular simulation. *J. Chem. Theory Comput.* **4**,
780   435-447 (2008).
781 65. Maier, J.A. et al. ff14SB: Improving the Accuracy of Protein Side Chain and Backbone
782   Parameters from ff99SB. *J Chem Theory Comput* **11**, 3696-713 (2015).
783 66. Melo, M.C.R., Bernardi, R.C., de la Fuente-Nunez, C. & Luthey-Schulten, Z. Generalized
784   correlation-based dynamical network analysis: a new high-performance approach for
785   identifying allosteric communications in molecular dynamics trajectories. *J Chem Phys*
786   **153**, 134104 (2020).
787 67. Romero-Rivera, A., Garcia-Borras, M. & Osuna, S. Role of Conformational Dynamics in
788   the Evolution of Retro-Aldolase Activity. *ACS Catal* **7**, 8524-8532 (2017).
789 68. Lange, O.F. & Grubmuller, H. Generalized correlation for biomolecular dynamics. *Proteins*
790   **62**, 1053-61 (2006).
791 69. Botello-Smith, W.M. & Luo, Y. Robust Determination of Protein Allosteric Signaling
792   Pathways. *J Chem Theory Comput* **15**, 2116-2126 (2019).
793 70. Anzalone, A.V. et al. Search-and-replace genome editing without double-strand breaks or
794   donor DNA. *Nature* **576**, 149-157 (2019).
795 71. K. A. Smolen, C.M.P., M. R. Swingle, A. Musiyenko, C. Li, A. D. Camp, R. E. Honkanen,
796   A. N Kettenbach. Quantitative proteomics and phosphoproteomics of PPP2R5D variants
797   reveal deregulation of RPS6 phosphorylation through converging signaling cascades. Vol.
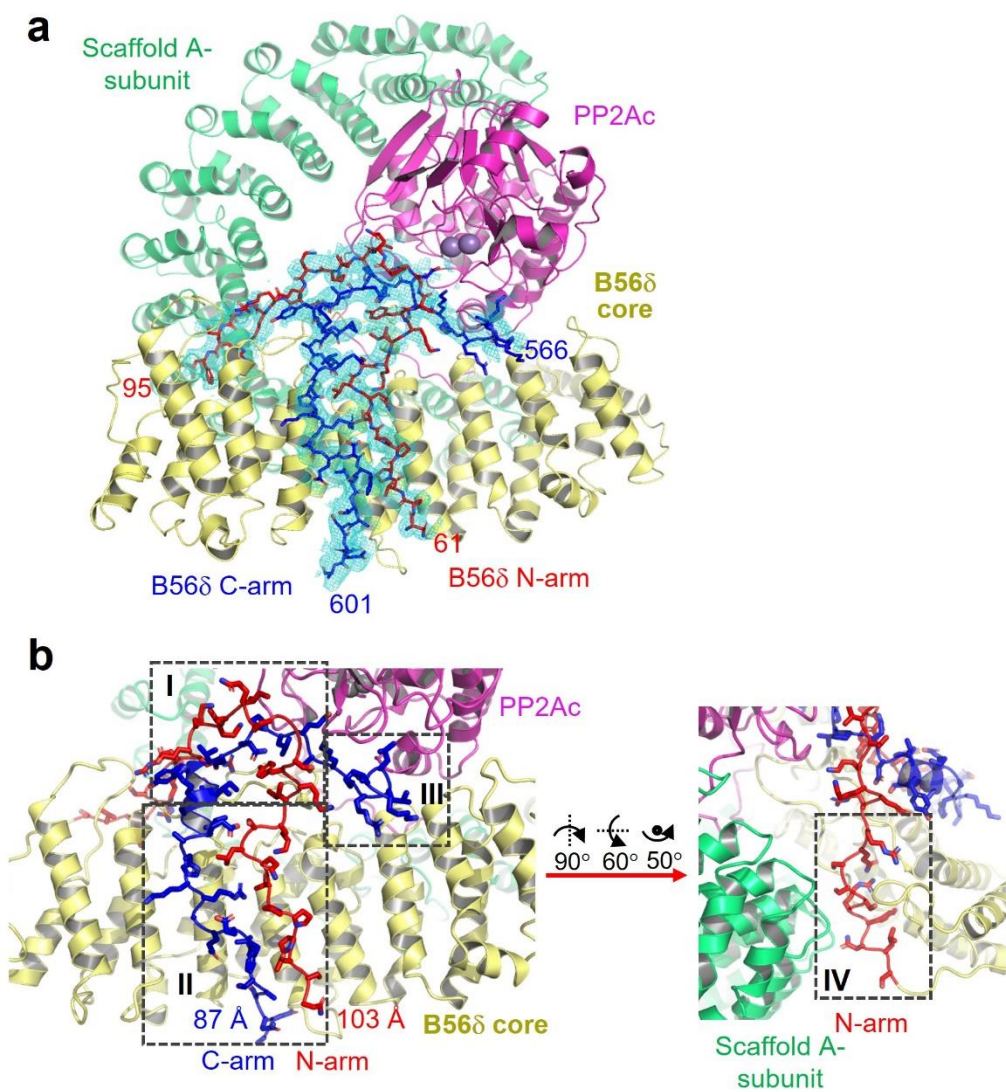798   https://www.biorxiv.org/content/10.1101/2023.03.27.534397v1 (bioRxiv, 2023).
799

806 **Figures and Table**

I: N/C-arm crossover-PP2Ac-B56-IL

	N/C	N-PP2Ac	C-PP2Ac	N-IL	C-IL
H-bonds	8	2	4	2	2
Hydrophobic	1	1			
salt bridge					1
unfavorable	1			2	2

II: N/C-arm-B56 core

	N/C	N-Core	C-Core-IL
H-bonds	3	4	8
Hydrophobic	5	2	5
salt bridge			
unfavorable			1

III: C-arm-PP2Ac-B56 core & IL

	C-PP2Ac	C-Core	C-IL
H-bonds		1	2
Hydrophobic	5	1	
salt bridge		1	1
unfavorable			

IV: N-arm-A-subunit-B56 core

	N-A	N-Core
H-bonds	3	8
Hydrophobic		3
salt bridge		1
unfavorable		2

807

808 **Figure 1.** The cryo-EM structure of the closed form of the E197K PP2A-B56δ holoenzyme. (a)

809 The overall cryo-EM structure of the E197K holoenzyme in the closed form. The A subunit,

810 PP2Ac, B56δ core, and N/C-arms are colored green, magenta, yellow, red, and blue,

811 respectively. The electron density map for N/C-arms is colored cyan. The N/C-arms are in sticks

812 and the rest of the structure is in cartoon. Manganese ions are shown in grey spheres. (b)

813 Mapping of the contact properties along the path of the super-dynamic interface spanning over

814 190 Å. The presentation of the structural model and the color scheme are the same as in (a).
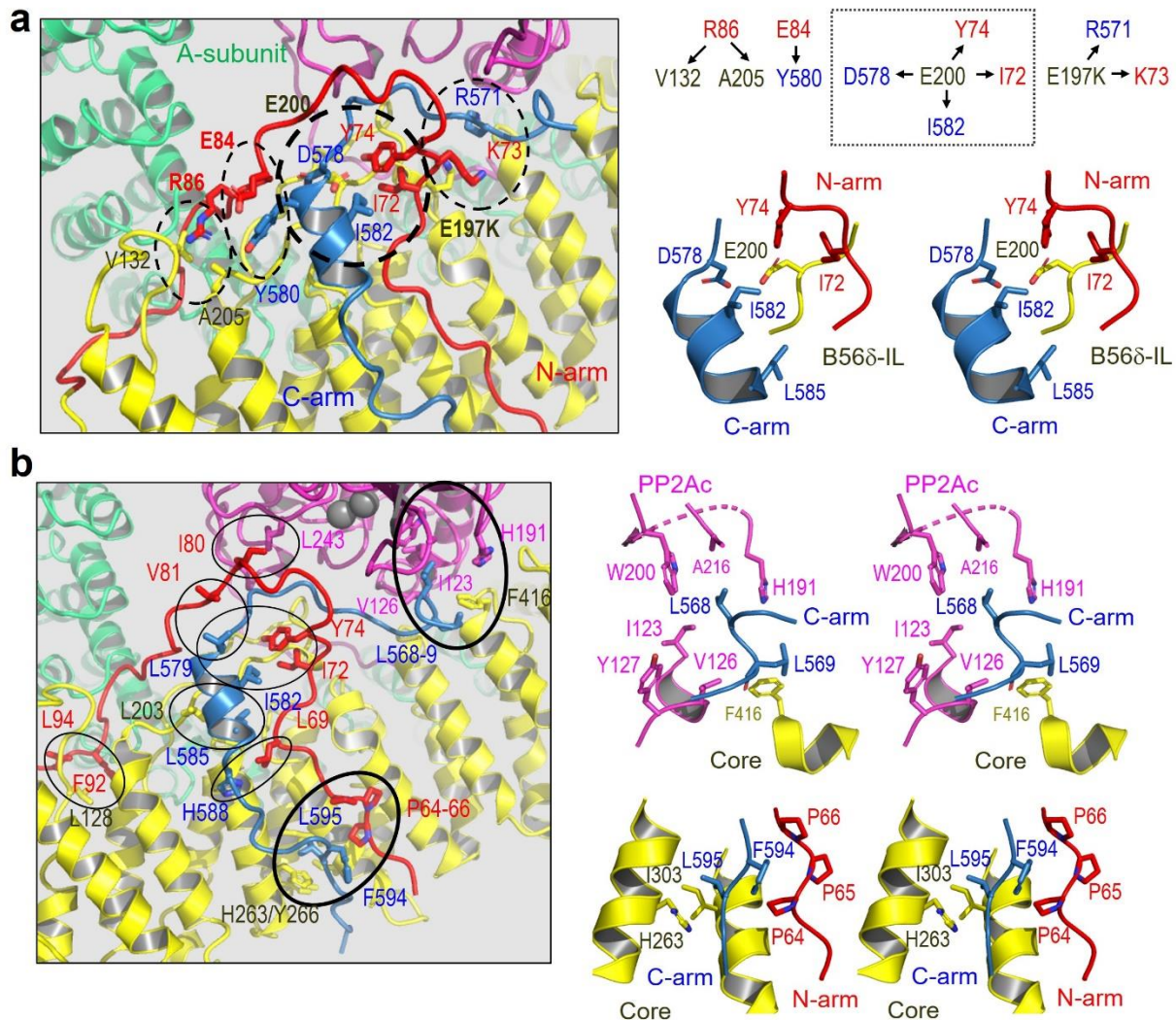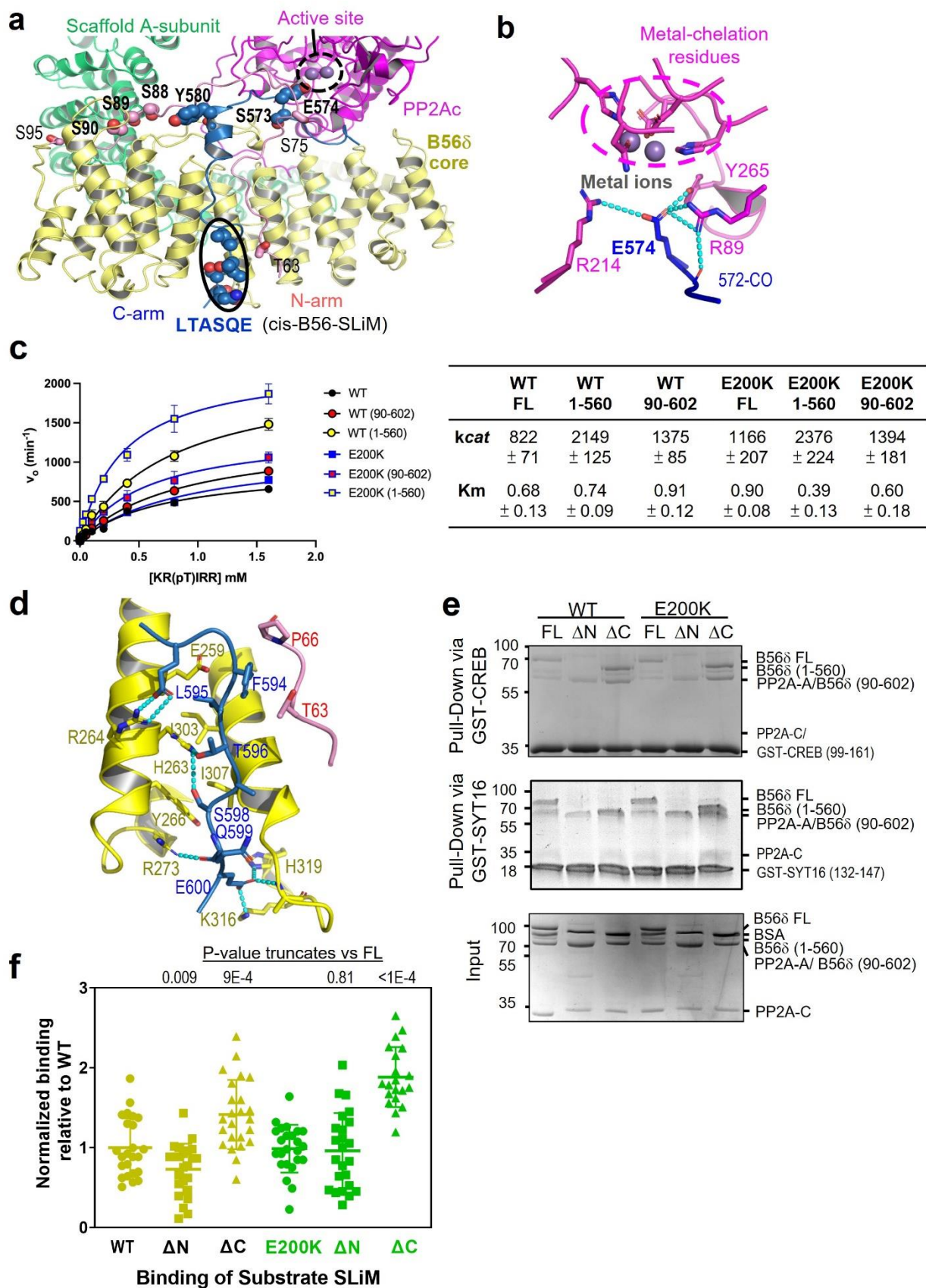
815

816

817

818

819

820

821

822

823

824

825

Figure 2. Mapping and closeup views of unfavoarable and hydrophobic contacts along the dynamic interface. (a) Distribution of unfavoarable and repulsive contacts at the dynamic interface, highlighted in dashed cycles (left) and illustrated at the upper right panel. The closeup stereoview of the central repulsive contacts with E200 is shown at the lower right panel. (b) Patches of hydrophobic contacts are in cycles and major hydrophobic interfaces are highlighted in thick cycles (left). The closeup stereoviews for the latter are shown (right). For (a-b), the color scheme is the same as in Fig.1. The structural models are shown in cartoon and key residues at the interfaces in sticks.

a Scaffold A-subunit; Active site; S89, S88, Y580; S90, S95; S573, E574; PP2Ac; B56δ core; S75; T63; C-arm; N-arm; LTASQE (cis-B56-SLiM)

b Metal-chelation residues; Metal ions; Y265; E574; R89; R214; 572-CO

c

	WT FL	**WT 1-560**	**WT 90-602**	**E200K FL**	**E200K 1-560**	**E200K 90-602**
kcat	822 ± 71	2149 ± 125	1375 ± 85	1166 ± 207	2376 ± 224	1394 ± 181
Km	0.68 ± 0.13	0.74 ± 0.09	0.91 ± 0.12	0.90 ± 0.08	0.39 ± 0.13	0.60 ± 0.18

d E259; P66; L595; F594; T63; R264; I303; H263; T596; I307; Y266; S598, Q599; R273; H319; E600; K316

e Pull-Down via GST-CREB; Pull-Down via GST-SYT16; Input; WT; E200K; FL ΔN ΔC; B56δ FL; B56δ (1-560); PP2A-A/B56δ (90-602); PP2A-C/ GST-CREB (99-161); GST-SYT16 (132-147); BSA; PP2A-C

f P-value truncates vs FL: 0.009 9E-4 0.81 <1E-4; Normalized binding relative to WT; WT ΔN ΔC E200K ΔN ΔC; Binding of Substrate SLiM

835

836 **Figure 3.** Structural mechanism of dual auto-inhibition and roles of the B56δ N/C-arms. (a) The

837 overall structure of the PP2A-B56δ holoenzyme highlights residues on the N/C-arms essential

838 for activation phosphorylation and suppressing the phosphatase active site and the SLiM-binding

839 groove. The structure is shown in cartoon and colored as in Fig. 1, except that the N/C-arms are

840 colored pink and blue, respectively. Residues with key regulation functions and manganese ions

841 (grey) are shown in spheres. (b) The closeup view of auto-inhibition at the phosphatase active

842 site. The active site metal ions are in spheres. Active site residues and E574 from the C-arm are

843 shown in sticks. (c) Truncations of either N- or C-arm increase the phosphatase activity of both

844 the WT and E200K holoenzymes. (d) The closeup view of auto-inhibition at the B56 SLiM-

845 binding groove, buttressed by extended interactions. (e) Examples of pulldown assays of the WT

846 and E200K PP2A-B56δ holoenzyme full length (FL), truncation of N-arm (ΔN) or C-arm (ΔC)

847 via GST-tagged CREB (99-161) (upper) or GST-SYT16 (132-147) (middle). One fifth of the

848 holoenzyme input is shown (lower). (f) All experimental repeats from (e) are normalized to the

849 WT holoenzyme, and the scatter plots of the normalized results, averages of all repeats, and

850 standard deviation (SD) are shown. The P-values for the full-length versus truncated

851 holoenzymes are calculated using Welch's t test. For (b) and (d), the structural models are shown

852 in cartoon, and the color scheme is the same as in (a). Residues at the interfaces are shown in

853 sticks. H-bond interactions are shown in cyan dashed lines.
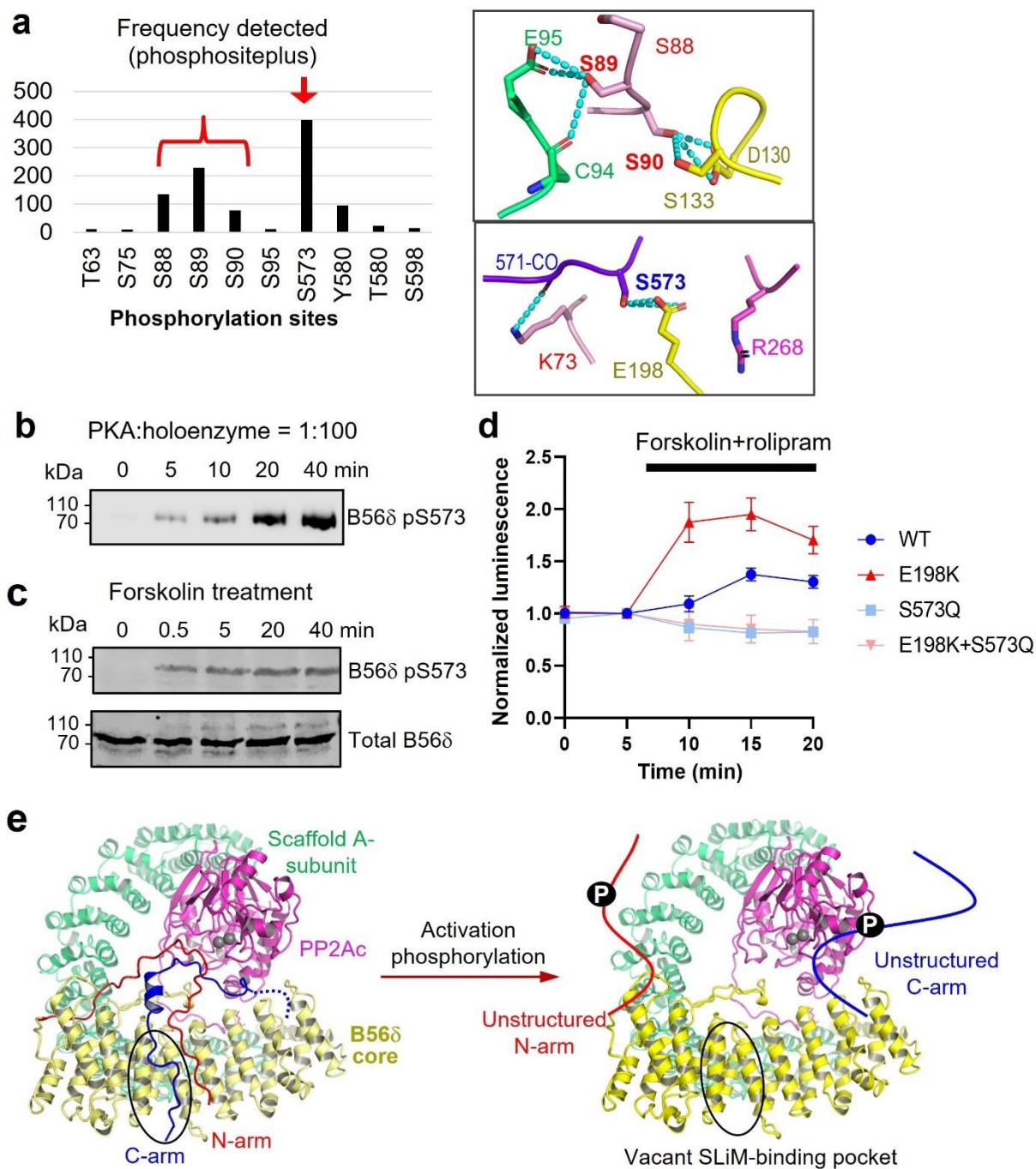
Figure 4. Structural mechanisms of activation phosphorylation of the PP2A-B56δ holoenzyme.

(a) The most frequently detected phosphorylation sites on the N/C-arms are highlighted (as

summarized from phosphosite.org) (left). The closeup views of these serine residues on the N/C-

arms and their interactions at the dynamic regulation interface (right). The color scheme is the

859   same as in Fig. 3a. Phosphorylation at these sites is expected to create repulsive contacts. (b)

860   Time-dependent changes in pS573 of the PP2A-B56δ holoenzyme by PKA *in vitro*. (c) Time-

861   dependent increase of B56δ pS573 upon cellular activation of cAMP/PKA. (d) Time-dependent

862   increase of substrate B56 SLiM binding the PP2A-B56δ holoenzyme (WT and E198K) in

863   mammalian cells upon cellular activation of cAMP/PKA by forskolin and rolipram. The non-

864   phosphorylatable mutation of B56δ, S573Q, abolishes this response. (e) Structural illustration of

865   phosphorylation-induced loosening of the N/C-arms for holoenzyme activation. Phosphorylation

866   of N/C-arms disrupts their interactions with the holoenzyme core, resulting in dual activation of

867   the phosphatase active site and the B56 SLiM-binding groove. The color scheme is the same as
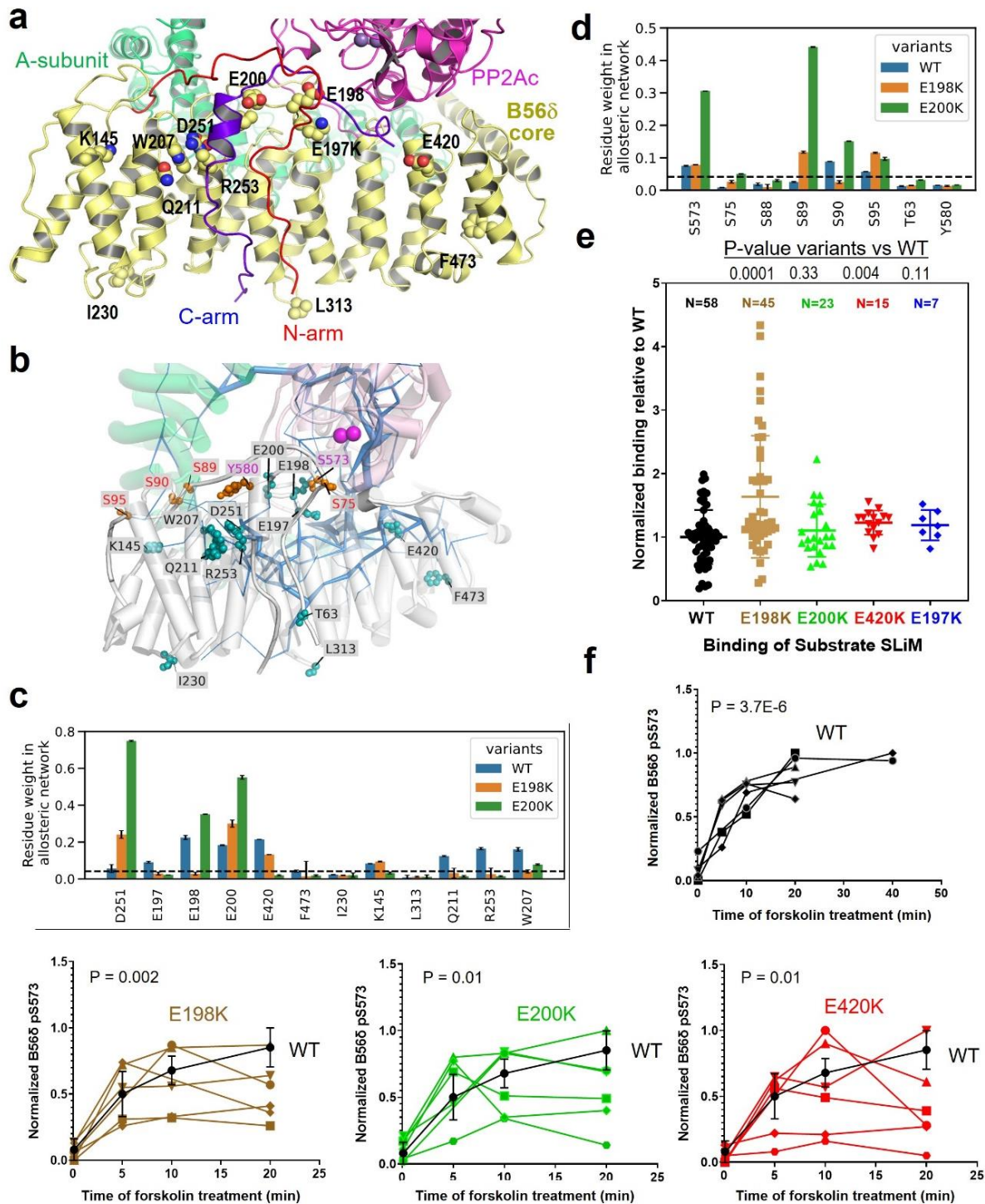
868   in Fig. 1.

869

870

871

872

873

874

875

876

Figure 5. The allosteric network of the PP2A-B56δ holoenzyme, perturbation by B56δ ID

mutations, and effects on holoenzyme functions. (a) The overall structure of the B56δ

holoenzyme highlights the B56δ ID residues predominantly located at the dynamic regulation

881   interface. (b) Illustration of the allosteric network of the PP2A-B56δ holoenzyme and its

882   relationship to ID residues (green ball-and-stick) and activation phosphorylation sites on N/C-

883   arms (orange ball-and-stick). The allosteric weights are shown as the thickness of blue wires.

884   They are estimated from REST2 simulations of the WT holoenzyme, modified from the cryo-EM

885   structure of the E197K holoenzyme in the closed form. (c-d) The global perturbation of residue

886   weights of ID residues and activation phosphorylation sites on the allosteric network by E198K

887   and E200K. The results in (b-d) are the average of 20 REST2 trajectories. (e) Pulldown of WT

888   and mutant holoenzymes by GST-tagged CREB (99-161) assessed the effects of ID mutations on

889   substrate SLiM binding. The data is normalized with the binding intensity of WT. The number of

890   repeats, their scatter plots, averages, and SD are shown. The P values for comparison of WT and

891   disease variants are calculated using Welch's t test. (f) Time-dependent phosphorylation of S573

892   in HEK293 cells expressing WT and mutant B56δ upon cellular cAMP/PKA stimulation. The

893   experiments were repeated six times. Means ± SD was calculated for WT for comparison to

894   disease variants. The P-values for time-dependent changes were calculated using Jonckheere-
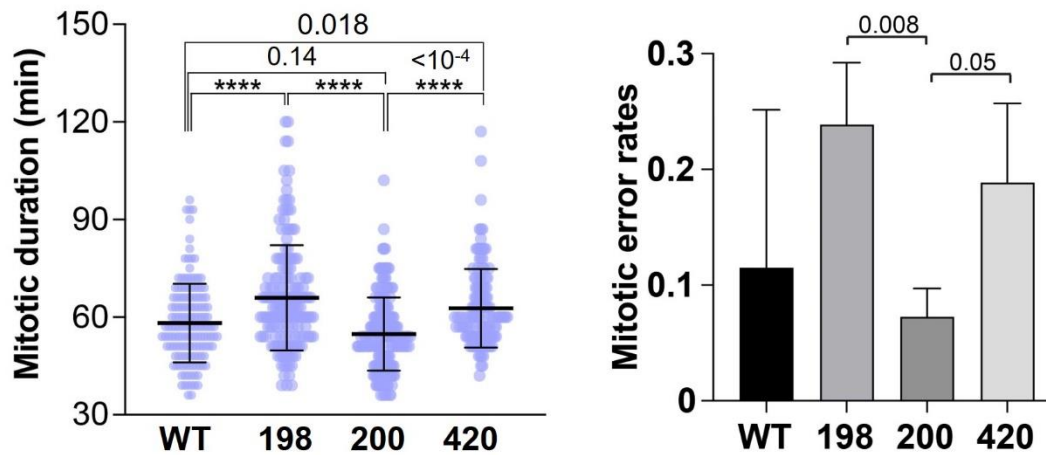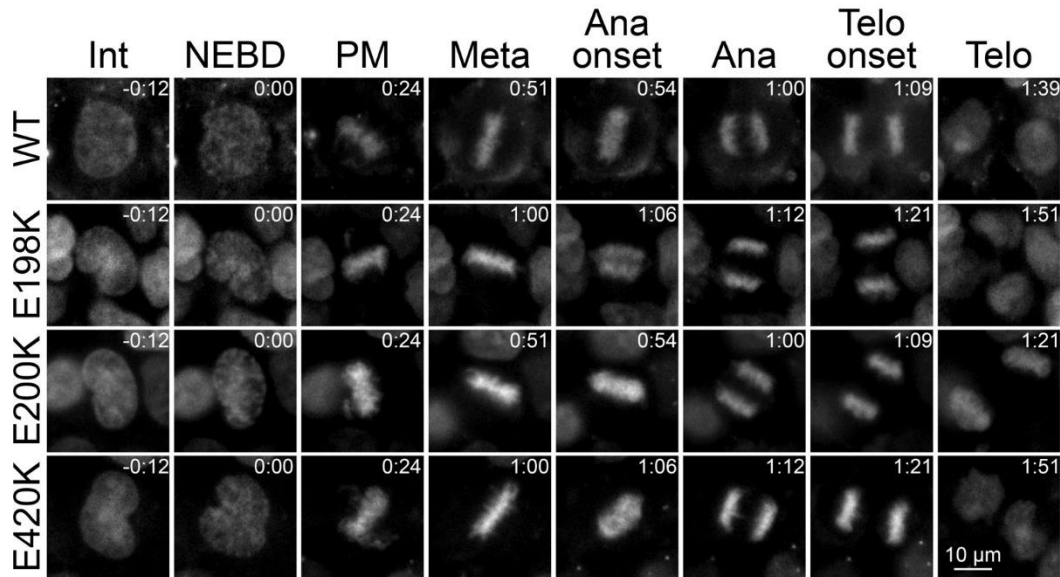
895   Terpstra test.

896

897

898

899

900

Figure 6. Effects of B56δ ID mutations on mitotic progression and mitotic errors. Representative live cell images of WT and B56δ ID mutant cells (E198K, E200K, and E420K) in HEK293 cells (top). Mitotic durations from NEBD to anaphase onset (bottom left) and the frequency of mitotic errors (bottom right) in the above cells are plotted. Means ± SD was calculated and shown. The P values for comparison of WT and disease variants are calculated using One-Way Anova (bottom, left) and two-tailed t-test (bottom, right). P-values <0.0001 are indicated by "****". N = 148, 162, 183 and 132 for WT, E198K, E200K and E420K cells.